Resolution Enhancement for Forward-Looking Imaging of Airborne Multichannel Radar via Space–Time Reiterative Superresolution

Lingyun Ren, Di Wu, and Daiyin Zhu, *Member, IEEE*

***Abstract*—In forward-looking imaging (FLI) of airborne radar, the enhancement of cross-range resolution is always a major research area and many studies on superresolution (SR) approaches, relied on the real array or virtual array, are proposed to break through the Rayleigh resolution. However, the reconstruction of complex scenes is still not accurate enough limited by the degrees of freedom. In this article, a novel FLI method for airborne multichannel radar named the space–time reiterative superresolution (ST-RISR) is proposed to obtain SR images of the forward-looking area, and hence to gain improved cross-range resolution. We first establish the space–time sampling model for airborne multichannel radar, where information in both the spatial and temporal slow-time domains is included, allowing for reconstructing more accurate SR images. In addition, the effect of array errors, always present in practice, is under consideration in the model. Then, a robust estimation algorithm called reiterative SR is employed and extended to process each of the so-called space–time snapshot in FLI. After the scattering coefficient vectors are obtained via the ST-RISR, they are accumulated to generate the final two-dimensional images. Finally, as is verified by simulated and measured data, the ST-RISR algorithm significantly improves the cross-range resolution of the forward-looking area, making it feasible in practical applications.**

***Index Terms*—Airborne multichannel radar, forward-looking imaging (FLI), reiterative superresolution (RISR), space–time signal processing, superresolution (SR) imaging.**

I. Introduction

FORWARD-LOOKING imaging (FLI) of airborne radar plays a vital role in many practical applications, such as complex terrain detection and aircraft blind landing, with the ability of generating 2-D images of the forward-looking areas in all weather conditions. Generally speaking, it is not hard to obtain high resolution in range by transmitting a special waveform, namely the chirp waveform, coupled with pulse compression techniques. However, the improvement of cross-range resolution is really a hard task for forward-looking airborne radar.

Received 6 April 2024; revised 15 June 2024; accepted 14 August 2024. Date of publication 21 August 2024; date of current version 5 September 2024. This work was supported in part by the Qing Lan Project of Jiangsu, China, and in part by the GuangDong Basic and Applied Basic Research Foundation under Grant 2024A1515011799. *(Corresponding author: Di Wu.)*

The authors are with the Key Laboratory of Radar Imaging and Microwave Photonics, Ministry of Education, College of Electronic and Information Engineering, Nanjing University of Aeronautics and Astronautics, Nanjing 211106, China, and also with the Shenzhen Research Institute, Nanjing University of Aeronautics and Astronautics, Nanjing 211106, China (e-mail: renlingyun@nuaa.edu.cn; wudi82@nuaa.edu.cn; zhudy@nuaa.edu.cn).

Digital Object Identifier 10.1109/JSTARS.2024.3446568

Existing high-resolution radar imaging technologies, such as synthetic aperture radar (SAR) and Doppler beam sharpen (DBS), are incapable of imaging in forward-looking area [1], [2]. The major reason is that the gradient of the Doppler frequency in this area is almost negligible, resulting in the difficulty to distinguish the scatterers located in different azimuth positions from the Doppler history. Moreover, the ambiguity of the Doppler history for symmetrical topographic points also deteriorates the performance of SAR or DBS. Thus, the real aperture radar (RAR), working in the scanning mode, can obtain rough forward-looking images via sweeping an antenna beam through the forward-looking area of the moving platform. Regrettably, the cross-range resolution is totally restricted by the beamwidth of the radar antenna, known as the Rayleigh limit, leading to a vast mismatch (several tens of times) between the range and cross-range resolutions [3].

To remedy the defect of the poor cross-range resolution, an amount of notable effort has been made in the past decades. Bistatic SAR systems, with separated transmitting and receiving platforms, may obtain satisfactory cross-range resolution in proper geometry. However, the high complexity of the systems, such as geometric configuration, time and frequency synchronization, limits its application in practice [4], [5].

Thus, most of the existing methods are based on monostatic systems, which consist of the following two types, i.e., deconvolution FLI methods for single-channel scanning radar systems, and superresolution (SR)-based algorithms for multichannel radar systems [6], [7], [8].

With the antenna beam sweeping in the forward-looking area, an azimuth signal model is established as the convolution of the antenna pattern and the scattering coefficients of the ground scene [9], [10]. Hence, the problem of FLI for single-channel scanning radar systems can be resolved by deconvolution methods when given the specific convolution kernel, i.e., antenna pattern. In the time domain, convolution is equivalent to establishing a set of linear equations and the target solution can be obtained by solving the equations [11]. However, from the viewpoint of signal recovery, deconvolution is known as a typically ill-conditioned inverse problem, making the reconstruction of ground truth very sensitive to noise. To alleviate that, a lot of efforts based on regularization have been made, such as the total variation sparse (TV-sparse) [12], Bayesian method [13], truncated singular value decomposition [14], and so on [15], [16], [17]. In the frequency domain, the convolution operation

between the target scattering coefficient and the antenna pattern is equivalent to low-pass filtering of the spectral function of the target. Therefore, the azimuth spectrum function of the target can be recovered by inverse filtering [18]. All these methods can improve the cross-range resolution of FLI to some extent, and some of them have been validated via measured data [19], [20].

The other kind of FLI methods is based on multichannel radar systems which employ array antenna aligned cross-track. The early works include the sector imaging radar for enhanced vision introduced by German Aerospace Center [21], and the monopulse FLI method for airborne radar [22]. The former improves the cross-range resolution via large physical aperture, and the latter introduces the monopulse angle estimation technique into the imaging to enhance the resolution of strong targets in the observed scene. Afterward, researchers attempted to introduce the SR spectral estimation techniques into array radar FLI, with a number of mature algorithms provided, such as Capon spectrum estimation, multiple signal classification (MUSIC), and many extensions to these methods [23], [24]. These methods also allow for achieving a resolution several times beyond the real-aperture beamwidth. In our previous work, we developed an improved MUSIC algorithm to cope well with correlated sources, and proved the feasibility of SR processing in airborne radar FLI through simulation and measured data. But this method needs a great deal of snapshots to accurately estimate the covariance matrix. Then, recently, some nonparametric estimation algorithms, such as the iterative adaptive approach (IAA) [25] and the iterative minimum mean-square error (MMSE), with the ability to cope with single snapshot, were applied in multichannel radar FLI to obtain good resolution performance [26], [27]. As it was verified by simulated data from an airborne phased-array radar system, these methods can improve the resolution in azimuth and overperform the monopulse imaging method in case of complex scenes.

In this article, we focus our research on resolution enhancement for FLI based on multichannel radar system. Considering the platform motion and antenna scanning, we present here a signal model of the targets in the forward-looking area received by the airborne multichannel radar. Based on this model, a space–time reiterative superresolution (ST-RISR) FLI algorithm is proposed for airborne multichannel radar, which intends to further improve resolution via space–time SR processing and gains better performance of imaging. On the one hand, the space–time snapshot, acquired by sampling in both the spatial and temporal (slow-time) domains, is regarded as the object to be SR processed instead of the spatial snapshot, which is expected to further improve the accuracy and resolution of SR estimation with additional temporal degrees of freedom (DoFs). On the other hand, the reiterative superresolution (RISR) is employed to achieve SR processing for each of the snapshot. Hence, the ST-RISR-based framework is proposed to resolve the imaging problem of forward-looking area. Besides, the effect of array errors, which is an inevitable factor in practice, is also involved in the framework. As is verified by simulations and measured data, the proposed ST-RISR algorithm significantly improves the cross-range resolution of the forward-looking area, and the image quality as well. Part of this work was presented in Ren et al. [27]'s work.

Overall, the main contributions of this article are presented as follows.

1) We started with the echo signal model of the targets in the forward-looking area received by the airborne multichannel radar, deeply analyzed the influence of platform motion and antenna scanning, and then provided expressions to describe the space–time signal model of the ground targets. In order to further improve the performance of the existing FLI methods, we extended the classic 1-D SR spectral estimation technique to the 2-D space–time domain, and thus proposed the ST-RISR algorithm to obtain the SR spectrum by processing the space–time snapshot in FLI, which is proved to be a feasible way to improve the performance of imaging.
2) Detailed analysis on the contribution to the improvement of cross-range resolution brought by the space–time processing to the SR-based FLI is present, making it possible for researchers to quantitatively analyze the performance of algorithm. We consider the effective length of the synthetic array caused by space–time processing, establishing the model of space–time equivalent array, and then use the length of the projection array as the evaluation metric. In combination with numerical calculation methods, the performance of space–time SR processing can be directly displayed, which can provide convenience to the follow-up research on the FLI technology based on multichannel radar.
3) Both the simulations results and experimental results are provided to verify the performance of the proposed ST-RISR FLI method in this article, showing its capability to achieve more accurate estimates, lower sidelobe, and obtain further resolution enhancement as well compared with the RAR imaging, the DBS and the FLI methods based on spatial spectral estimation.

The rest of this article is organized as follows. In Section II, the echo signal model of the targets in the forward-looking area is established for multichannel airborne array radar. In Section III, a 2-D ST-RISR algorithm is proposed to address the problem of poor cross-range resolution and hence improve the performance of FLI. In Section IV, simulated data and measured data are employed to validate the proposed ST-RISR-based FLI algorithm. Finally, Section V concludes this article.

II. Echo Analysis and Multichannel Signal Model

The 3-D geometry of data collection for airborne multichannel radar is shown in Fig. 1. A narrow-band forward-looking radar, flying with velocity v and altitude H, with array antennas aligned cross-track is under consideration. The array antenna beam circularly scans through the forward-looking area with the scanning velocity ω, and at the same time, the radar transmits a burst of linear frequency modulated pulses at certain pulse repetition frequency (PRF). A single ground scatterer, denoted by P in Fig. 1, is localized in the imaging area and within the mainlobe of the radar beam. Assume that the number of

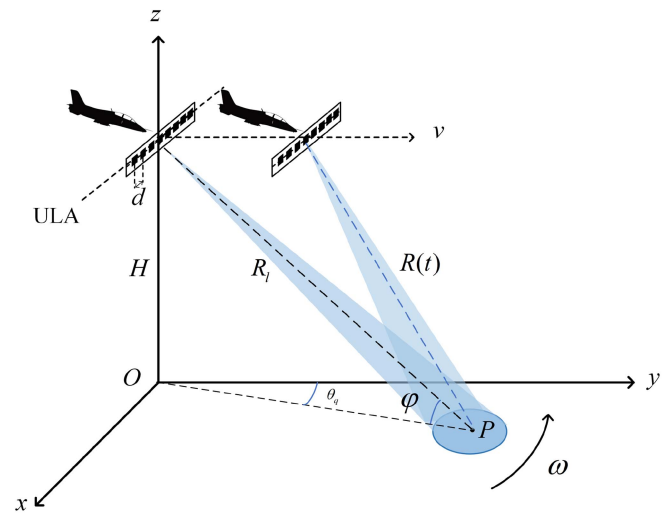

Fig. 1. 3-D geometry for airborne multichannel radar FLI.

range gates and the predetermined azimuth grids in the FLI area are L and Q, with l and q representing the indexes of them, respectively. Let R_l, θ_q, and φ denote the range, azimuth angle and pitch angle of target P with respect to the radar. The number of receiving channels (subarrays) and the distance between adjacent receiving channels are M and d. After range pulse compression and migration correction, the baseband received signal of the mth channel is given by

$$s(\tau,t,m)=\sigma(R_l,\theta_q)h\left(t-\frac{\theta_q}{\omega}\right)s\left(\tau-\frac{2R_l}{c}\right)\times\exp\left\{-j\frac{2\pi}{\lambda}[2R(t)+md\sin\theta_q\cos\varphi]\right\} \quad (1)$$

where $\sigma(R_l,\theta_q)$ represents the scattering coefficient of the target P, and τ, t, λ stand for the fast-time, the slow-time, the wavelength, respectively. The function $h(\cdot)$ and $s(\cdot)$ indicate the two-way antenna pattern modulation and the point spread function, i.e., the transmitted waveform after pulse compression.

The instantaneous range *R(t)* from *P* to the radar reference point varies with the movement of platform, which can be formulated as

$$R(t)=\sqrt{{R_l}^2+(vt)^2-2R_lvt\cos\theta_q\cos\varphi}. \quad (2)$$

After Taylor expansion of the above-mentioned equation, we have

$$R(t)=R_l-vt\cos\theta_q\cos\varphi+\frac{1-\cos^2\theta_q\cos^2\varphi}{2R_l}v^2t^2+O(t^2). \quad (3)$$

Generally speaking, the quadratic terms and infinitely small quantities of higher order terms can be ignored due to long operating range, so the above-mentioned equation can be approximated as

$$R(t)=R_l-vt\cos\theta_q\cos\varphi. \quad (4)$$

Substituting (4) into (1), and omitting the constant term caused by R_l, we obtain

$$s(\tau,t,m)=\sigma(R_l,\theta_q)h\left(t-\frac{\theta_q}{\omega}\right)s\left(\tau-\frac{2R_l}{c}\right)\times\exp\left\{j\frac{4\pi vt}{\lambda}\cos\theta_q\cos\varphi\right\}\times\exp\left\{-j\frac{2\pi md}{\lambda}\sin\theta_q\cos\varphi\right\}. \quad (5)$$

Assume that a total number of N pulses are transmitted and received during a single imaging processing period, and the number of the received fast-time samples is L. Hence the complex baseband samples comprise an $L\times N\times M$ datacube. To simultaneously utilize both the spatial sampling obtained by multichannel receiving and the temporal sampling obtained by coherent pulses, the 3-D data block is divided into K subblocks in slow-time, each of which contains the echo from N'successive pulses in a coherent processing interval (CPI), typically assumed to be 4–32 considering the beam scanning, and will be processed coherently. Thus, after periodically sampling in azimuth at the rate of f_R, the discrete received signal in the lth range gate and the kth CPI is given by

$$s(n,m)=\sum_{q=1}^{Q}\sigma(\theta_q)h(\theta_q-\bar{\theta}_k)e^{j2\pi\bar{f}_d(\theta_q)n}e^{-j2\pi\bar{f}_s(\theta_q)m} \quad (6)$$

where n is the index of pulses in a CPI, and $\bar{\theta}_k$ represents the azimuth boresight direction of the beam at the central pulse of the kth subblock. Note that, since the number of pulses in each CPI is relatively small, the change of antenna pattern weighting between pulses are ignored, i.e., the weight induced by antenna pattern is regarded as a constant within CPI. Defining the normalized Doppler frequency and spatial frequency as

$$\bar{f}_d(\theta_q)=\frac{2v}{\lambda f_R}\cos\theta_q\cos\varphi \quad (7)$$

$$\bar{f}_s(\theta_q)=\frac{d}{\lambda}\sin\theta_q\cos\varphi. \quad (8)$$

To avoid spatial aliasing, the boundary of azimuth angle is given by [28]

$$\theta_b=\sin^{-1}\left(\frac{\lambda}{2d\cos\varphi}\right). \quad (9)$$

For the scatterer located at the azimuth position θ_q, the corresponding $M\times 1$ spatial steering vector and the $N'\times 1$ temporal steering vector are denoted by

$$\mathbf{a}_s(\theta_q)=\left[e^{-j2\pi\bar{f}_s(\theta_q)},\ldots,e^{-j2\pi M\bar{f}_s(\theta_q)}\right]^{\mathrm{T}} \quad (10)$$

and

$$\mathbf{a}_t(\theta_q)=\left[\mathrm{e}^{j2\pi\bar{f}_d(\theta_q)},\ldots,\mathrm{e}^{j2N'\pi\bar{f}_d(\theta_q)}\right]^{\mathrm{T}} \quad (11)$$

respectively.

Hence, the space–time steering vector with respect to the azimuth position θ_q is expressed as

$$\mathbf{a}(\theta_q)=\mathbf{a}_t(\theta_q)\otimes\mathbf{a}_s(\theta_q) \quad (12)$$

where $\otimes$ denotes the Kronecker product, and superscript T stands for the operation of transposition.

The discrete received signal in (6) is assembled in the form of a column vector of size $MN' \times 1$ expressed as $\mathrm{vec}(\mathbf{s}_{l,k})$, which is known as the so-called space–time snapshot. Then, (6) can be rewritten as a vector form given by

$$\mathrm{vec}(\mathbf{s}_{l,k}) = \sum_{\theta=\bar{\theta}_k-\theta_b}^{\bar{\theta}_k+\theta_b} \sigma(\theta_q) h(\theta_q - \bar{\theta}_k)\mathbf{a}(\theta_q) + \mathbf{n} \tag{13}$$

where $\mathbf{n}$ stands for the noise component at each of the temporal and spatial samples, which is independent with other components.

By introducing the notation of matrix, (13) can be rewritten as

$$\mathrm{vec}(\mathbf{s}_{l,k}) = \mathbf{A}\mathbf{x}_{l,k} + \mathbf{n} \tag{14}$$

where $\mathbf{x}_{l,k}$ is the vector of scattering coefficient for the discrete scatterers weighted by the antenna pattern. Letting Q' denote the length of scattering coefficient vector $\mathbf{x}_{l,k}$, the $MN' \times Q'$ space–time steering matrix $\mathbf{A}$ is expressed as

$$\mathbf{A} = [\mathbf{a}(\bar{\theta}_k - \theta_b), \ldots, \mathbf{a}(\bar{\theta}_k + \theta_b)]^{\mathrm{T}}. \tag{15}$$

It is worth noting that more precise angular grid quantization is produced by larger value of Q', and then enhance the SR capability.

Considering the inevitable modeling errors in practice, such as the uncertainty of channel location and mutual coupling effects, the received space–time snapshot is expressed as

$$\mathrm{vec}(\mathbf{s}_{l,k}) = (\mathbf{A}\mathbf{x}_{l,k}) \odot \mathbf{z} + \mathbf{n} \tag{16}$$

where $\odot$ is the Hadamard product, $\mathbf{z}$ represents the modeling errors, the ith random deviation of which is modeled as

$$\Delta_i = 1 + \Delta_{ai} \exp(j\Delta_{\varphi i}) \tag{17}$$

where Δ_{ai} and $\Delta_{\varphi i}$ is the random amplitude and phase deviation of the ith element with variance σ_z^2.

In this way, the spatial samples and the temporal samples, obtained by the multiple channels and successive coherent pulses, respectively, form the space–time snapshots, which are used for FLI of airborne multichannel radar. From (8), the reconstruction of $\mathbf{x}_{l,k}$ from the obtained space–time snapshot is reformulated as the problem of spatial angular spectral estimation. A coarse result of $\mathbf{x}_{l,k}$ can be obtained by matching filtering, which is denoted by

$$\mathbf{x}_{l,k} = \mathbf{A}^{\mathrm{H}}\mathrm{vec}(\mathbf{s}_{l,k}) \tag{18}$$

where $\{\}^{\mathrm{H}}$ is conjugate transpose operation.

III. Proposed Airborne Multichannel Radar FLI Method

A. Iterative MMSE Algorithm

The MMSE-based iterative algorithm was first derived in radar pulse compression to suppress the range sidelobe induced by match filtering to the noise level, and then reveal the small scatterers hidden nearby. The approach determines the specific receiving filter for each range cell by updating the filter coefficients that matches the real echo adaptively [29]. Motivated by the performance of adaptive pulse compression, then the algorithm was extended to direction of arrival (DOA) estimation named as RISR to complete source localization, with benefits such as operation with low snapshot, robustness to coherent sources, and severe noise [30].

Assume that the narrow-band signal impinges on the far-field uniform linear array (ULA), so the received signal $\mathbf{y}(t)$ at time t can be modeled as

$$\mathbf{y}(t) = \mathbf{S}\mathbf{x}(t) + \mathbf{n}(t) \tag{19}$$

where $\mathbf{S}$ is the array manifold matrix composed of the spatial steering vectors expressed as (10).

The RISR algorithm establishes the MMSE cost function and determines the weighting filter coefficient $\mathbf{W}$ by minimizing it, which is expressed as

$$\min E\left\{\left\|\mathbf{x}(t) - \mathbf{W}^{\mathrm{H}}\mathbf{y}(t)\right\|^2\right\}. \tag{20}$$

Then, yields the MMSE weighting filter

$$\mathbf{W} = \left(E\left\{\mathbf{y}(t)\mathbf{y}^{\mathrm{H}}(t)\right\}\right)^{-1} E\left\{\mathbf{y}(t)\mathbf{x}^{\mathrm{H}}(t)\right\}. \tag{21}$$

Substituting (19) into (21), and assuming the noise is independent of the signal component, with covariance matrix denoted by $\mathbf{R}_n = E\{\mathbf{n}(t)\mathbf{n}^{\mathrm{H}}(t)\}$, then we obtain

$$\mathbf{W} = (\mathbf{S}\mathbf{P}\mathbf{S}^{\mathrm{H}} + \mathbf{R}_n)^{-1}\mathbf{S}\mathbf{P} \tag{22}$$

where $\mathbf{P}$ is the spatial power distribution matrix, which is a diagonal matrix with diagonal elements expressed as $E\{\mathbf{x}(t)\mathbf{x}^{\mathrm{H}}(t)\}$. As can be seen from (22), the calculation of MMSE weighting filter depends on the $\mathbf{x}(t)$ to be estimated, which is not available in advance, hence we need to employ matching filtering to obtain rough estimate first.

B. Space–Time RISR

To overcome the limitation of physical length of antenna array, with (22) applied to the spatial snapshots received by the array aligned cross-track, the distribution of target can be reconstructed via spatial SR processing, and then the forward-looking image is obtained via projection. It is worth noting that the algorithm improves the cross-range resolution of scatterers to an extent. But the number of DoFs is restricted by the size of array for airborne radar, the improvement is limited for point-like targets and the contour of important area, and especially the performance deteriorates for complex forward-looking scene.

In this section, we extend the spatial SR processing to the space–time domain and thereby propose the space–time RISR focusing on the further enhancement of cross-range resolution. Based on the proposed space–time FLI model in Section II, the algorithm introduces the additional temporal DoFs in SR processing and gains higher ability to resolve targets within the beam.

In the space–time RISR, the initial estimation of $\mathbf{x}_{l,k}$ is obtained from the matched filter processing expressed as

$$\hat{\mathbf{x}}_{l,k} = \mathbf{A}^{\mathrm{H}}\mathrm{vec}(\mathbf{s}_{l,k}). \tag{23}$$

Algorithm 1: Space-Time RISR Algorithm.

Require:
The space-time snapshot: $(\mathbf{s}_{l,k})$
The $MN' \times Q'$ space-time steering matrix $\mathbf{A}$
Ensure:
Initialization: $\mathbf{x}_{l,k} = \mathbf{A}^{\mathrm{H}}\mathrm{vec}(\mathbf{s}_{l,k})$;
Calculate the initial spatial power distribution matrix;
Determine the power of noise and calculate the noise covariance matrix;
if the termination condition is not met **then**
Calculate the MMSE weighting filter
$\mathbf{W} = (\mathbf{A}\hat{\mathbf{P}}_{l,k}\mathbf{A}^{\mathrm{H}} + \sigma_n^2\mathbf{I}_{MN'\times MN'})^{-1}\mathbf{A}\hat{\mathbf{P}}_{l,k}$
Calculate the estimation result of $\mathbf{x}_{l,k}$
$\hat{\mathbf{x}}_{l,k} = \mathbf{W}^{\mathrm{H}}\mathrm{vec}(s_{l,k})$
Update the spatial power distribution matrix $\mathbf{x}_{l,k}$
else
Obtain the final estimation for the vector of scattering coefficient $\hat{\mathbf{x}}_{l,k} = \sqrt{\hat{\mathbf{P}}_{l,k}}$;
end if
return The estimation result $\hat{\mathbf{x}}_{l,k}$;

Then, define the spatial power distribution matrix as

$$\hat{\mathbf{P}}_{l,k} = [\hat{\mathbf{x}}_{l,k}\hat{\mathbf{x}}_{l,k}^{\mathrm{H}}] \odot \mathbf{I}_{Q'\times Q'} \tag{24}$$

where $\mathbf{I}_{Q'\times Q'}$ is an identity matrix of size $Q' \times Q'$.

The relatively accurate estimation of $\mathbf{x}_{l,k}$ can be obtained by the minimization of the MMSE cost function, which is computed as

$$\hat{\mathbf{x}}_{l,k} = \left[\left(\mathbf{A}\hat{\mathbf{P}}_{l,k}\mathbf{A}^{\mathrm{H}} + \sigma_n^2\mathbf{I}_{MN'\times MN'}\right)^{-1}\mathbf{A}\hat{\mathbf{P}}_{l,k}\right]^{\mathrm{H}}\mathrm{vec}(\mathbf{s}_{l,k}) \tag{25}$$

where σ_n^2 is the power of noise, which is assumed to be additive Gaussian white noise. Then, the result of (25) is applied in (24) to update the spatial power distribution matrix. The recursive structure of (25) determines that it can be solved iteratively, i.e., the previous estimation of spatial power distribution matrix is applied in (25) to compute the new estimation of scattering coefficient until convergence. The termination condition can be set as

$$\|\hat{\mathbf{x}}_{l,k}(i) - \hat{\mathbf{x}}_{l,k}(i-1)\|^2 < \varepsilon \tag{26}$$

where i is the number of iteration, ε is the preset value (acceptable error).

We now consider to recover the scattering coefficients in the presence of modeling errors, which is inevitable in practice, and demonstrate the robustness of ST-RISR algorithm with the effects of modeling errors. The MMSE weighting filter becomes

$$\hat{\mathbf{W}} = \left(\mathbf{A}\hat{\mathbf{P}}_{l,k}\mathbf{A}^{\mathrm{H}} + \mathbf{R}_z + \sigma_n^2\mathbf{I}_{MN'\times MN'}\right)^{-1}\mathbf{A}\hat{\mathbf{P}}_{l,k} \tag{27}$$

where $\mathbf{R}_z$ is the uncertainty covariance matrix caused by modeling errors, which can be denoted by Ren et al. [27]

$$\mathbf{R}_z = \sigma_z^2\mathbf{I}_{MN'\times MN'} \odot (\mathbf{A}\hat{\mathbf{P}}_{l,k}\mathbf{A}^{\mathrm{H}}). \tag{28}$$

Note that the modeling error term and the additive noise term are both diagonal matrices, so the impact of them in (27) can be regarded as regularization, which is an effective way to resolve the problem of eigenvalue dispersion for signal covariance matrix and eliminate the ill-conditional problem in proposed ST-RISR algorithm. In practice, noise power and modeling error variance are not known prior. To resolve this issue, an adaptive diagonal matrix Σ is employed to replace the total covariance matrix $\mathbf{R}_z + \mathbf{R}$. Hence, (27) is slightly modified as

$$\hat{\mathbf{W}} = \left(\mathbf{A}\hat{\mathbf{P}}_{l,k}\mathbf{A}^{\mathrm{H}} + \Sigma\right)^{-1}\mathbf{A}\hat{\mathbf{P}}_{l,k}. \tag{29}$$

The noise power estimate can be calculated by [31]

$$\hat{\sigma}_n^2 = \frac{1}{MN'}\sum_{i=1}^{MN'}\left|\frac{\mathbf{i}_i^{\mathrm{H}}(\mathbf{A}\hat{\mathbf{P}}_{l,k}\mathbf{A}^{\mathrm{H}})^{-1}\mathrm{vec}(\mathbf{s}_{l,k})}{\mathbf{i}_i^{\mathrm{H}}(\mathbf{A}\hat{\mathbf{P}}_{l,k}\mathbf{A}^{\mathrm{H}})^{-1}\mathbf{i}_i}\right|^2 \tag{30}$$

where $\mathbf{i}_i$ is the ith column of the identity matrix $\mathbf{I}_{MN'\times MN'}$. The model error variance σ_z^2, determined by an acceptable model error tolerance, is empirically set to –30 dB of the peak signal power.

As derived previously, the conventional array processing based on spatial-only dimension is extended to 2-D space–time processing. After several iterations, typically 5–10, we obtain the SR reconstructed scattering coefficient vector for the lth range gate and kth subblock.

C. ST-RISR-Based FLI Framework

After obtaining the estimation of one scattering coefficient vector, the next step is to accumulate it to the final image matrix according to its current beam center position, which is expressed as

$$I\left(l,\bar{\theta}_k\right) = I\left(l,\bar{\theta}_k\right) + |\mathbf{x}_{l,k}|, \bar{\theta}_k - \theta_b < \theta < \bar{\theta}_k + \theta_b. \tag{31}$$

Thus, the proposed FLI method for airborne multichannel radar generates the final 2-D image by two steps. First, applying the ST-RISR algorithm to the space–time snapshots one by one in the sampling data block to obtain the scattering coefficient vector of each snapshot. And then accumulate them according to their ranges and beam centers to generate the final 2-D images. Fig. 2 demonstrates the entire imaging processing flowchart.

Since the temporal dimension is introduced into the SR processing in the ST-RISR algorithm, the number of data points per snapshot is increased from M to MN' as compared to the spatial-only SR method. Thus, for an identical scenario to be imaged, the ST-RISR-based FLI method gains higher ability to resolve targets within the beam, yielding better performance for FLI.

D. Equivalent Array

The spatial SR spectral estimation can break through the Rayleigh limit, but its performance is still depended on the size of real or virtual antenna. There is no doubt that the resolution for

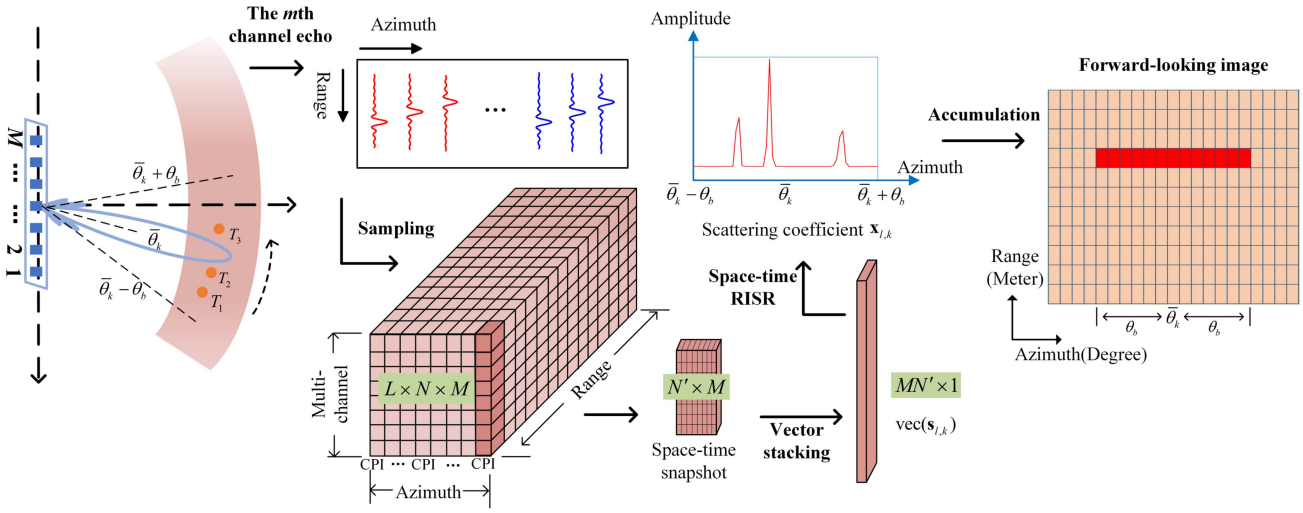

Fig. 2. Demonstration of the FLI method.

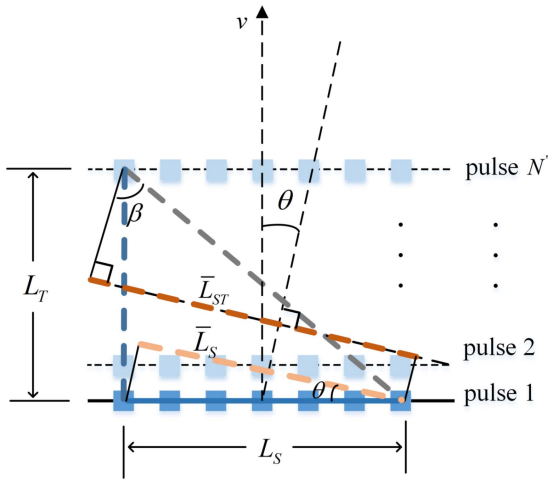

Fig. 3. Demonstrations of the effective length of SR processing.

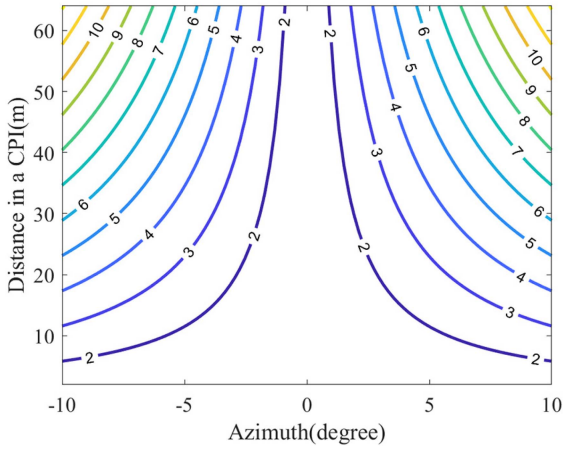

Fig. 4. Increment of effective length by space–time SR processing.

both the real aperture imaging and the SR imaging is improved with the size of antenna increasing.

As we know, for fixed value of the wavelength, the beamwidth is mainly determined by the length of the effective equivalent array, i.e., the length of projection array perpendicular to the boresight direction θ, which can be expressed as

$$\bar{L}_S = L_S \cos\theta \tag{32}$$

where L_S and $\bar{L}_S$ denote the real and effective lengths of the array, respectively.

Therefore, the length of the projection array can be used as an evaluation metric for SR spectral estimation. Compared with forward-looking method based on spatial SR spectral estimation, the proposed model introduces additional temporal DOFs to generate azimuth SR spectrum, which contributes to a certain increase of the length of equivalent array. Fig. 3 shows the geometry of the effective length in case of space–time processing, where the ULA is mounted on a moving platform, and the echo is collected in a CPI consistent of N' pulses. As we can see, by coherently processing of the pulses, a synthetic rectangular array is generated during the flight of the platform and the length of the array is corresponding to the temporal DoFs, which is denoted by

$$L_T = N' T_R v \tag{33}$$

where T_R stands for the pulse repetition interval.

It can be seen that the spatial sampling capability of airborne radar along with platform motion is characterized by the spatial array mapping of the space–time model, and the physical mechanism of airborne radar SR imaging is described more intuitively. The SR imaging of scanning beam of airborne radar is transformed into the DOA estimation problem of the virtual array mapped perpendicular to the boresight direction. Now, we consider the effective length of the synthetic array with respect to θ caused by the space–time processing, which can be

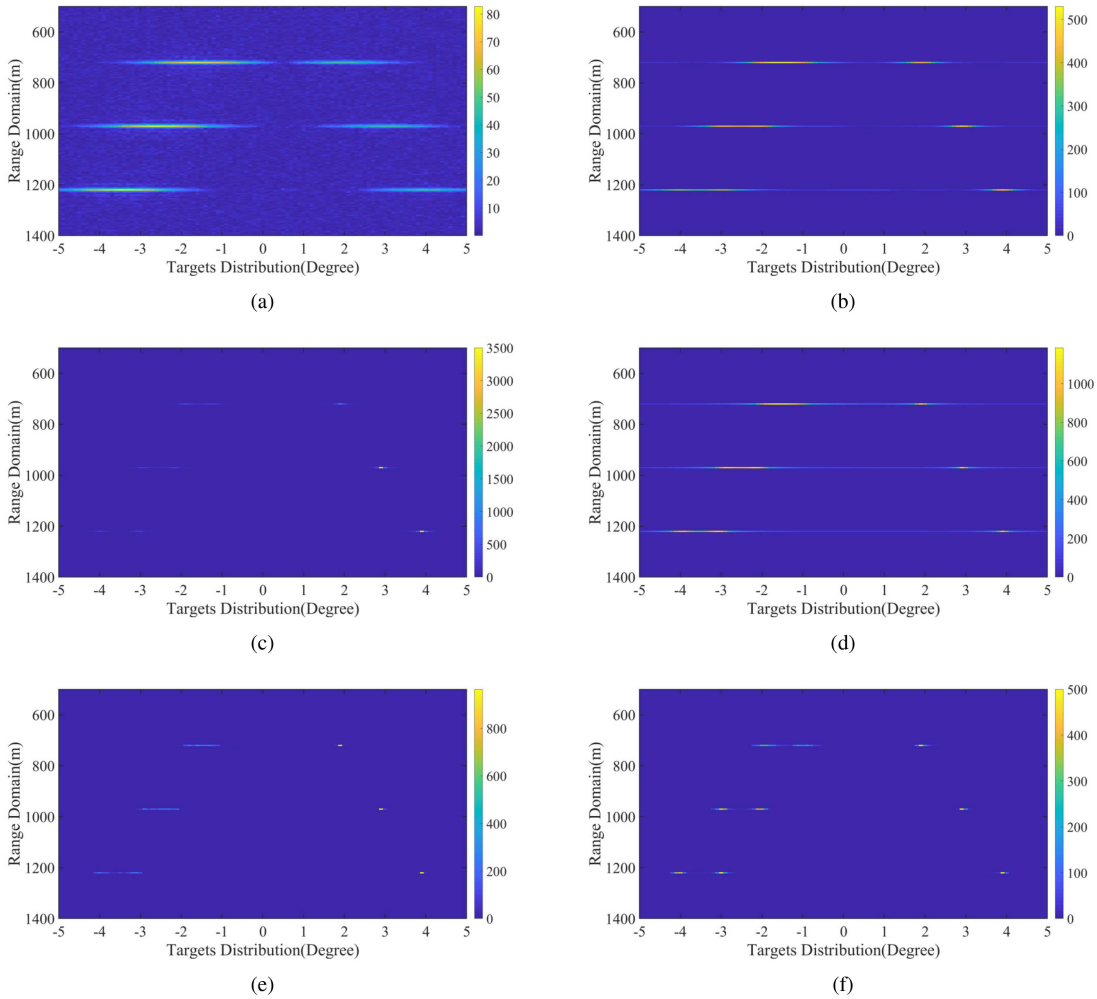

Fig. 5. Results for the simulation scenario. (a) Real beam image. (b) Imaging result of SPICE algorithm. (c) Imaging result of music algorithm. (d) Imaging result of IAA algorithm. (e) Imaging result of OMP algorithm. (f) Imaging result of ST-RISR algorithm.

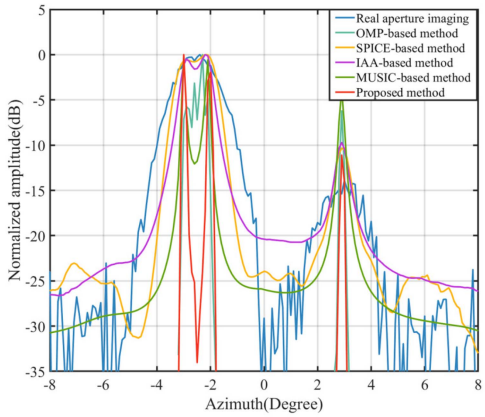

Fig. 6. Results for the point targets simulation.

expressed as

$$\bar{L}_{ST} = \sqrt{L_T^2 + L_S^2}\sin(\theta + \beta) \tag{34}$$

where β is calculated by

$$\beta = \mathrm{tg}^{-1}\left(\frac{L_S}{L_T}\right). \tag{35}$$

Substituting (35) into (34), we obtain

$$\bar{L}_{ST} = \sqrt{L_T^2 + L_S^2}\sin\left[|\theta| + \mathrm{tg}^{-1}\left(\frac{L_S}{L_T}\right)\right]. \tag{36}$$

From (32) and (36), it is obvious that when employing space–time SR processing, the effective length of the array is the synthetic rectangular array oriented perpendicular to the beam center. Therefore, we now evaluate the increment of the effective length of ULA brought by space–time SR processing against L_T and θ for fixed value of the real array length. In Fig. 4, the 2-D contour image shows the normalized increment of the effective length, which is defined as

$$\Delta\bar{L}_{ST} = \frac{\bar{L}_{ST}}{\bar{L}_S}. \tag{37}$$

As we can see from Fig. 4, the effective length of the array increases with the CPI increasing, indicating an improved azimuth

TABLE I
PARAMETERS OF SIMULATION

Parameter	Value
Wavelength	0.03 m
Bandwidth	40 MHz
Platform speed	100 m/s
Beam scanning speed	100 ° /s
PRF	1000 Hz
Number of receiving channels	8
Distance between each channel	0.06 m
Number of coherent processing pulses	8
SNR	25 dB

TABLE II
PARAMETERS OF SIMULATION

Parameter	Value(scenario1)	Value(scenario2)
Wavelength	0.03 m	0.03 m
Bandwidth	40 MHz	40 MHz
Platform speed	100 m/s	80 m/s
Beam scanning speed	120 °/s	120 °/s
PRF	1000 Hz	1000 Hz
Number of receiving channels	8	8
Distance between receiving channels	0.045 m	0.12 m
Number of coherent processing pulses	16	16
Scan range	–20°-20°	–30°-30°

resolution of the FLI. Besides, the increment of effective length for the scatters deviating from the forward-looking direction is larger.

IV. Simulation and Experimental Results

In this section, both the simulations results and experimental results are provided to verify the performance of the proposed ST-RISR FLI method. We first compare the proposed FLI method based on the space–time signal model with the FLI algorithms based on spatial SR spectral estimation. Then, the advantage of the proposed space–time SR FLI algorithm is tested via simulated scenario, and the measured data as well. In the simulation, we defined the signal-to-noise ratio (SNR) as

$$\mathrm{SNR} = 10\log_{10}\frac{P_s}{P_n} \tag{38}$$

where P_s is the peak power of the data after pulse compression, P_n is the power of the additive Gaussian white noise denoted by $P_n = \sigma_n^2$. In the simulation and measured data processing, the number of iterations is preset as 10.

A. Point-Target Simulation Results

First, the effectiveness of the proposed method is verified by the simulation of point targets. The scene is composed of nine point targets, each three of which are located at the same range gate. The simulation parameters are displayed in Table I. Fig. 5 shows the imaging results of the real aperture imaging method, four spatial SR-based FLI methods including the OMP, MUISC, IAA, and SPICE-based FLI method, and also the proposed ST-RISR FLI method. Each of the plots is obtained via averaging over 100 Monte-Carlo trials.

The real aperture imaging result is shown in Fig. 5(a). The 3 dB width of the real beam is about 2.2°. Because of the limitation of the beamwidth of antenna, two close targets on degree apart in the same range cell cannot be distinguished after real aperture imaging. The imaging results from the SR methods based on SPICE, MUISC, IAA, and OMP are presented in Fig. 5(b)–(e). All the SR imaging methods are illustrated with the ability of higher cross-range resolution, which can resolve the two adjacent targets within the main beamwidth to a certain extent. The results show that the FLI imaging method based on SPICE algorithm and IAA algorithm improve the cross-range resolution and suppress the noise. However, the sidelobe of the reconstructed point-targets is relatively high. The FLI imaging method based on MUSIC algorithm has better performance of distinguishing the two targets localized at –3 and –2°, but the estimation of the target amplitude is distorted. The OMP-based FLI method is very suitable for the resolution enhancement of isolated, strong, point-like target. However, the capability of angle estimation becomes invalid when there are multiple targets in the beam, or even widely distributed targets, which leads to poor resolution and even false targets in imaging processing. Generally, the above-mentioned problems are caused by insufficient DOFs in spatial processing. Owing to the more advanced space–time signal model, the space–time SR-based algorithms gain more DoFs than the existing spatial SR imaging algorithm. After space–time RISR imaging processing, three targets in the same range cell are clearly located, which prove that the algorithm can effectively distinguish multiple targets in the main lobe, and provide feasibility for airborne radar forward imaging.

In Fig. 6, the azimuth profiles of the three point targets in 256th range gate are presented. As we can see, the real aperture imaging and OMP-based FLI method fail to distinguish the two targets localized at –3 and –2°, whose interval is less than the beamwidth of the radar antenna. MUISC, IAA, and SPICE-based FLI methods can slightly resolve the two adjacent targets. By contrast, the proposed FLI method based on ST-RISR has the capability to achieve further resolution enhancement with lower sidelobe, and obtain more accurate estimates as well.

B. Surface-Target Simulation Results

Then, the advantage of the proposed ST-RISR-based FLI algorithm is verified via simulated scenarios. Two existing high-resolution SAR images are selected as the simulation backgrounds, as shown in the Figs. 7(a) and 10(a), respectively. To generate the echoes from an airborne forward-looking multichannel radar, each of the pixels in the 2-D SAR image is seen as a ground scatterer, with the corresponding complex value being the reflectivity. Then, the echo signals from all the ground scatterers are summed up and the white Gaussian noise with SNR of 20 dB is added to the echo. The simulation parameters are displayed in the Table II to simulate forward-looking multichannel echo signals to validate the proposed FLI method.

The first scenario includes some lanes and buildings in a town. The azimuth covers for –20 to 20° and the range covers

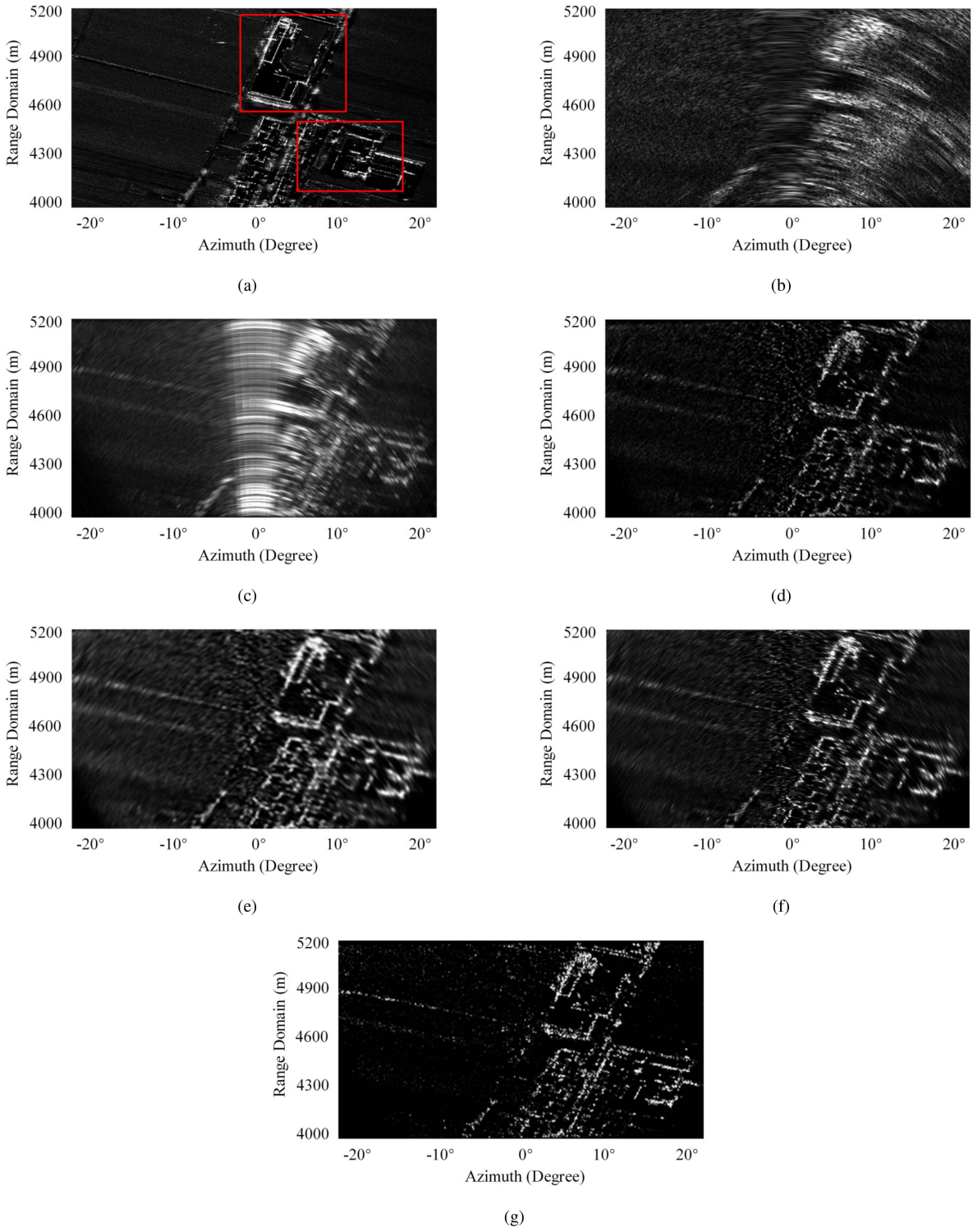

Fig. 7. Results for the simulation scenario. (a) SAR image (background). (b) Real beam image. (c) Imaging result of DBS. (d) Imaging result of OMP-based method. (e) Imaging result of IAA-based method. (f) Imaging result of space-RISR-based method. (g) Imaging result of ST-RISR method.

from 4000 to 5200 m. Six FLI methods, i.e., the real aperture imaging, DBS imaging, the IAA-based imaging, the OMP-based imaging, space RISR-based imaging and space–time RISR-based imaging methods, are employed to process the simulated datasets.

The result of real aperture imaging is shown in Fig. 7(b), where the point targets are obviously blurred, and the contour features of the surface target are fuzzy. In Fig. 7(c), the DBS technique can obtain imaging of squint-looking area, regretfully, fails to FLI, where the poor imaging performance caused by the

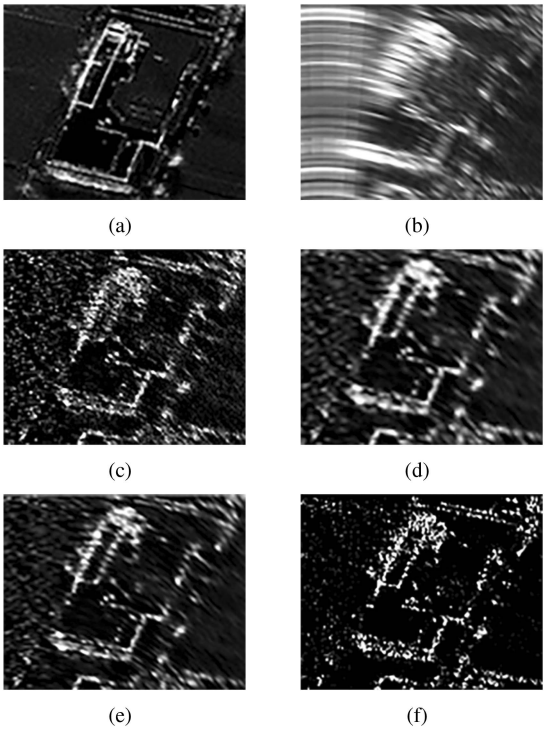

Fig. 8. Enlarged image of zone 1. (a) SAR image (background). (b) Real beam image. (c) OMP. (d) IAA. (e) Space-RISR. (f) ST-RISR method.

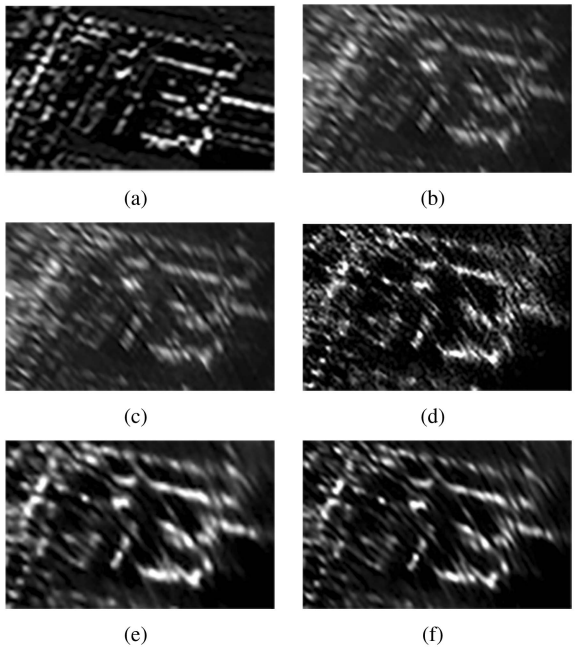

Fig. 9. Enlarged image of zone 2. (a) SAR image (background). (b) Real beam image. (c) OMP. (d) IAA. (e) Space-RISR. (f) ST-RISR method.

small gradient of Doppler frequency is clearly seen. Fig. 7(d)–(e) illustrates the results of OMP and IAA-based FLI methods. As seen, the cross-resolution can be improved by all the methods. However, The OMP-based method misestimates with the inaccurate presetting sparsity and hard to recover the surface targets. The IAA-based method suffers from higher sidelobes. In Fig. 7(f)–(g), we apply the RLSR algorithm to FLI and present the imaging results via the RISR method and the space–time RISR based on the proposed FLI model. Compared with other SR algorithms, the RISR algorithm achieves more accurate estimation and low sidelobe. Moreover, space–time RISR shows a stronger ability to suppress background noise and sidelobe, and obtain higher cross-range resolution for both point targets and the surface targets as well. To clearly shown the details of the images, we enlarged a same part of the images from difference methods in Figs. 8 and 9.

The second scenario includes some runways in an airport. We still process the simulated data via the above-mentioned algorithms, and show the results in Fig. 10. It can be seen that real aperture imaging cannot distinguish point targets, such as aircrafts, nor restore the outline of buildings and all the three methods can provide images with improved the azimuth resolution as compared to the real aperture imaging method. By comparing these images, we find that the improvement of the DBS imaging is really limited. The comparison of spatial SR and space–time SR imaging results proves that the image scene can be reconstructed more accurately and the contour features of buildings can be effectively improved by effectively utilizing the Doppler frequency information generated by the relative motion between moving platform and target. For a more intuitive comparison, Figs. 11 and 12 are enlarged images of two sets of details.

TABLE III
MAIN RADAR SYSTEM PARAMETERS

Parameter	Value
Radar band	X band
Platform speed	145 m/s
PRF	450 Hz
Number of receiving channels	4
Distance between each channel	0.14 m
Number of coherent processing pulses	4
Main-lobe beam width	2.7°
Scan range	−20°-20°

C. Measured Data Processing

In this section, the improved performance of the proposed method is further validated by a group of measured data collected by an X-band airborne multichannel radar. The radar systems have four independent receiving channels, and work in forward-looking scanning mode. The major parameters are listed in Table III.

The scenario of interest is from a mountain region. Fig. 13(a) shows the real aperture imaging result, wherein the scatterers clearly blurred due to the poor cross-range resolution. The traditional monopulse method can obtain finer cross-range resolution to some extent, as shown in Fig. 13(b), for those isolated, strong, point-like targets particularly. However, the contour of the land is missed.

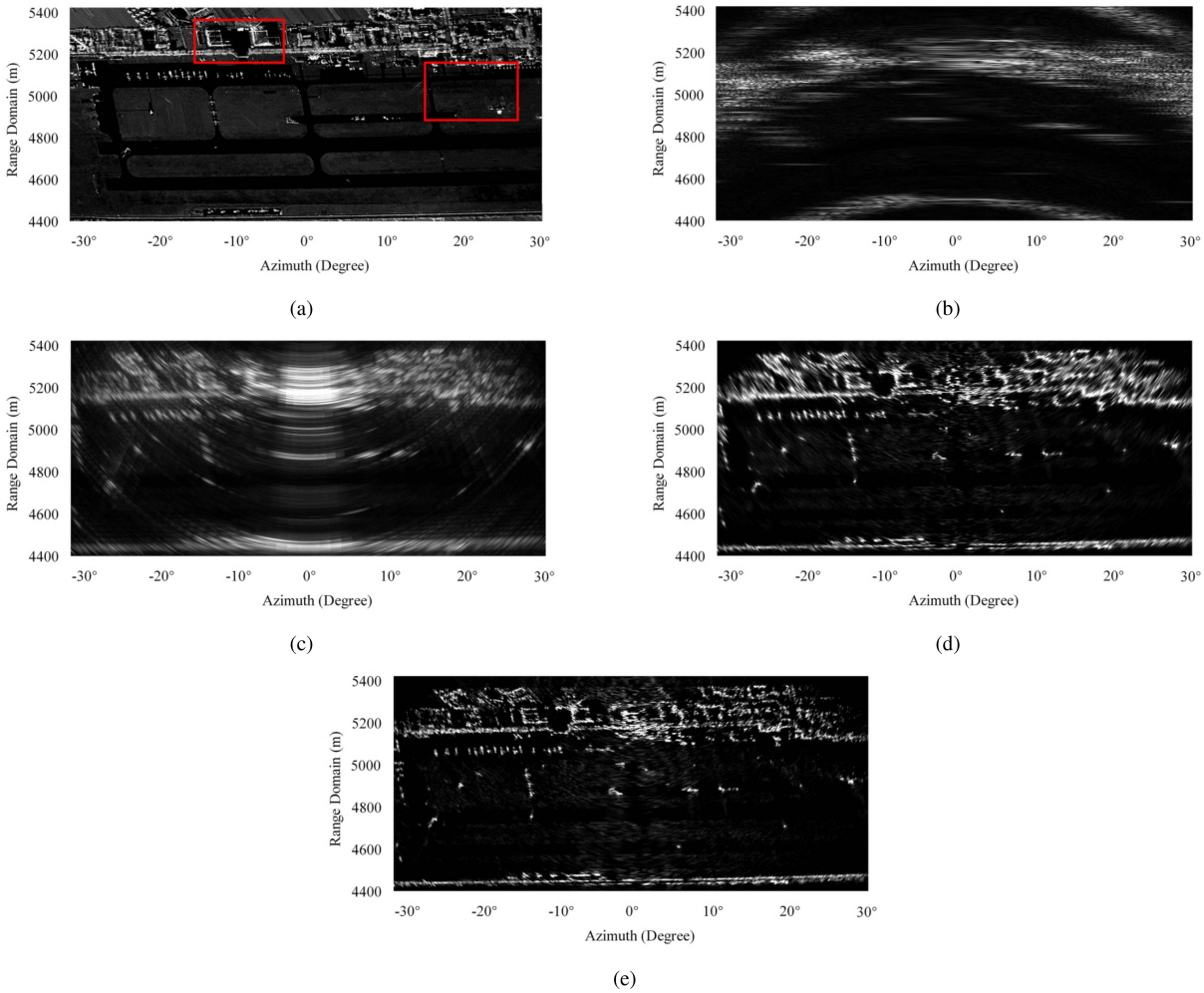

Fig. 10. Results for the simulation scenario. (a) SAR image (background). (b) Real beam image. (c) DBS. (d) Space-RISR. (e) ST-RISR method.

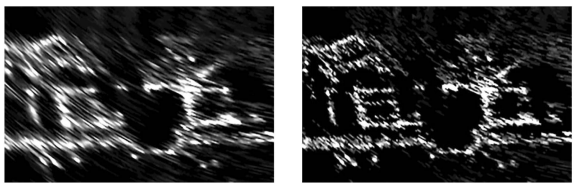

(a) (b)

Fig. 11. Enlarged image of zone 1. (a) Space-RISR. (b) ST-RISR method.

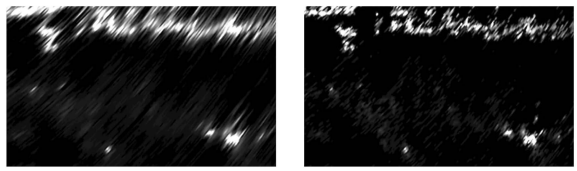

(a) (b)

Fig. 12. Enlarged image of zone 2. (a) Space-RISR. (b) ST-RISR method.

In Fig. 13(b), the imaging result are obtained by the OMP-based FLI method. It can be seen that, the azimuth resolution is improved, particularly for those isolated and strong point targets.

Fig. 13(c) shows the imaging result of the RISR algorithm, which can achieve higher resolution than the real aperture imaging method and the OMP-based FLI method. In contrast, the imaging result of the proposed space–time RISR-based FLI method is provided in Fig. 13(d), with the core of applying the RISR algorithm on the received space–time snapshot. It is clear that the scenario is better reconstructed with higher cross-range resolution and clearer terrain profile.

TABLE IV
ENTROPY AND CONTRAST OF MEASURED DATA

Methods	Entropy	Contrast
Real-aperture image	4.718	0.1177
OMP-based method	2.1530	0.1280
Spatial RISR-based method	2.1061	0.1683
The proposed ST-RISR method	1.6571	0.1865

Besides, from the perspective of image entropy and contrast, as shown in the Table IV, the proposed FLI method is indicated

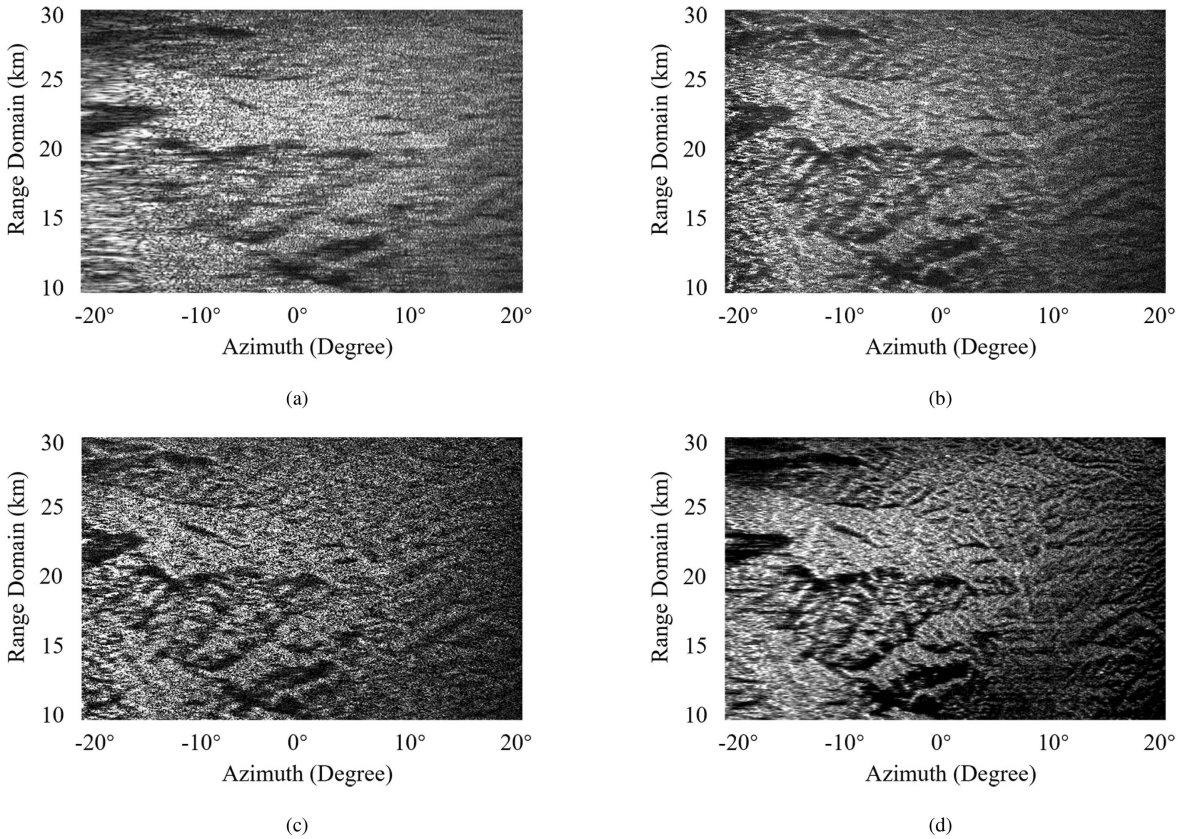

Fig. 13. FLI results for the measured mountain region. (a) Real beam image. (b) Imaging result of OMP. (c) Imaging result of space RISR. (d) Imaging result of the proposed ST-RISR method.

to obtain clearer SR image than other methods with the lowest image entropy and the highest contrast.

V. Conclusion

In this article, a novel space–time RISR-based FLI method was proposed to improve the cross-range resolution for airborne multichannel radar. In this method, the SR processing is applied on the 2-D data sampled in both spatial and temporal domains, wherein the spatial sampling is achieved by multichannel receiving technique, while the temporal sampling is achieved by receiving a ground of coherent pulses. By adopting adaptive array signal processing, multichannel radar system gains the ability to improve the azimuth resolution, and by introducing the slow-time domain to imaging, we obtained a more accurate SR image via increasing the DOFs. The proposed method was evaluated by the scenario simulation and the measured data processing results, which proved its superiority compared with current multichannel radar FLI algorithms, and applicability in practical processing.

References

[1] A. Moreira, P. Prats-Iraola, M. Younis, G. Krieger, I. Hajnsek, and K. P. Papathanassiou, "A tutorial on synthetic aperture radar," *IEEE Geosci. Remote Sens. Mag.*, vol. 1, no. 1, pp. 6–43, Mar. 2013.

[2] E. Onat and Y. Özkazanç, "An analysis of Doppler beam sharpening technique used in fighter aircraft," in *Proc. 2018 26th Signal Process. Commun. Appl. Conf. (Siu)*, 2018, pp. 1–4.

[3] W. R. Alpers, D. B. Ross, and C. L. Rufenach, "On the detectability of ocean surface waves by real and synthetic aperture radar," *J. Geophys. Res.: Oceans*, vol. 86, no. C7, pp. 6481–6498, 2012.

[4] J. Yang et al., "A first experiment of airborne bistatic forward-looking SAR-preliminary results," in *Proc. 2013 IEEE Int. Geosci. Remote Sens. Symp.-IGARSS*, Conference Proceedings, IEEE, 2013, pp. 4202–4204.

[5] H. Mei et al., "Thorough understanding property of bistatic forward-looking high-speed maneuvering platform SAR," *IEEE Trans. Aerosp. Electron. Syst.*, vol. 53, no. 4, pp. 1826–1845, Aug. 2017.

[6] S. Uttam and N. A. Goodman, "Superresolution of coherent sources in real-beam data," *IEEE Trans. Aerosp. Electron. Syst.*, vol. 46, no. 3, pp. 1557–1566, Jul. 2010.

[7] M. A. Richards, "Iterative noncoherent angular superresolution (radar)," in *Proc. 1988 IEEE Nat. Radar Conf.*, 1988, pp. 100–105.

[8] A. Quinquis, E. Radoi, and F. C. Totir, "Some radar imagery results using superresolution techniques," *IEEE Trans. Antennas Propag.*, vol. 52, no. 5, pp. 1230–1244, May 2004.

[9] D. Mao et al., "Angular superresolution of real aperture radar with high-dimensional data: Normalized projection array model and adaptive reconstruction," *IEEE Trans. Geosci. Remote Sens.*, vol. 60, pp. 1–16, 2022.

[10] Y. Zhang, W. Li, Y. Zhang, Y. Huang, and J. Yang, "A fast iterative adaptive approach for scanning radar angular superresolution," *IEEE J. Sel. Top. Appl. Earth Obs. Remote Sens.*, vol. 8, no. 11, pp. 5336–5345, Nov. 2015.

[11] Y. Zhang, Y. Zhang, Y. Huang, W. Li, and J. Yang, "Angular superresolution for scanning radar with improved regularized iterative adaptive approach," *IEEE Geosci. Remote Sens. Lett.*, vol. 13, no. 6, pp. 846–850, Jun. 2016.

[12] Q. Zhang et al., "TV-sparse super-resolution method for radar forward-looking imaging," *IEEE Trans. Geosci. Remote Sens.*, vol. 58, no. 9, pp. 6534–6549, Sep. 2020.

[13] H. Chen et al., "Bayesian forward-looking superresolution imaging using doppler deconvolution in expanded beam space for high-speed platform," *IEEE Trans. Geosci. Remote Sens.*, vol. 60, pp. 1–13, 2022.

[14] X. Tuo, Y. Zhang, Y. Huang, and J. Yang, "Fast sparse-TSVD super-resolution method of real aperture radar forward-looking imaging," *IEEE Trans. Geosci. Remote Sens.*, vol. 59, no. 8, pp. 6609–6620, Aug. 2021.

[15] D. Mao et al., "Angular superresolution of real aperture radar for target scale measurement using a generalized hybrid regularization approach," *IEEE Trans. Geosci. Remote Sens.*, vol. 61, pp. 1–14, 2023.
[16] J. Tang, Z. Liu, L. Ran, R. Xie, and J. Qin, "Enhancing forward-looking image resolution: Combining low-rank and sparsity priors," *IEEE Trans. Geosci. Remote Sens.*, vol. 61, pp. 1–12, 2023.
[17] X. Tuo, D. Mao, Y. Zhang, Y. Zhang, Y. Huang, and J. Yang, "Radar forward-looking super-resolution imaging using a two-step regularization strategy," *IEEE J. Sel. Top. Appl. Earth Obs. Remote Sens.*, vol. 16, pp. 4218–4231, 2023.
[18] Y. Zhang, Y. Zhang, W. Li, Y. Huang, and J. Yang, "Super-resolution surface mapping for scanning radar: Inverse filtering based on the fast iterative adaptive approach," *IEEE Trans. Geosci. Remote Sens.*, vol. 56, no. 1, pp. 127–144, Jan. 2018.
[19] Y. Li, J. Liu, X. Jiang, and X. Huang, "Angular superresol for signal model in coherent scanning radars," *IEEE Trans. Aerosp. Electron. Syst.*, vol. 55, no. 6, pp. 3103–3116, Dec. 2019.
[20] J. Xia, X. Lu, and W. Chen, "Multi-channel deconvolution for forward-looking phase array radar imaging," *Remote Sens.*, vol. 9, no. 7, pp. 703–728, 2017.
[21] G. Krieger, J. Mittermayer, M. Wendler, F. Witte, and A. Moreira, "SIREV - sector imaging radar for enhanced vision," in *Proc. ISPA 2001: Proc. 2nd Int. Symp. Image Signal Process. Anal.*, 2001, pp. 377–382.
[22] T. Zhou, B. Pang, D. Dai, H. Wu, and X. Wang, "Monopulse forward-looking imaging algorithm based on Levenberg–Marquardt optimisation," *J. Eng.*, vol. 2019, no. 20, pp. 6593–6597, 2019.
[23] J. Zhang, D. Wu, D. Zhu, and P. Jiang, "An airborne/missile-borne array radar forward-looking imaging algorithm based on super-resolution method," in *Proc. IEEE 2017 10th Int. Congr. Image Signal Process., BioMedical Eng. Inform.*, 2017, pp. 1–5.
[24] G. H. Zhao, Y. W. Fu, and Z. W. Zhuang, "Imaging by root-MUSIC for forward looking radar with linear array," in *Proc. 2013 Int. Conf. Wireless Commun. Signal Process.*, 2013, pp. 1–6.
[25] T. Yardibi, J. Li, P. Stoica, M. Xue, and A. B. Baggeroer, "Source localization and sensing: A nonparametric iterative adaptive approach based on weighted least squares," *IEEE Trans. Aerosp. Electron. Syst.*, vol. 46, no. 1, pp. 425–443, Jan. 2010.
[26] R. Chen, W. Li, K. Li, Y. Zhang, and J. Yang, "A super-resolution scheme for multichannel radar forward-looking imaging considering failure channels and motion error," *IEEE Geosci. Remote Sens. Lett.*, vol. 20, pp. 1–5, 2023.
[27] L. Ren, D. Wu, M. Liu, and D. Zhu, "A space-time iterative adaptive method for forward-looking radar imaging," in *Proc. 2021 CIE Int. Conf. Radar, Conf. Proc.*, 2021, pp. 298–301.
[28] C. Ren, X. Wang, Z. Xue, and J. Liu, "Investigation on grating lobe suppression of uniform antenna array," in *Proc. 2011 IEEE Int. Conf. Microw. Technol. Comput. Electromagnetics*, 2011, pp. 285–288.
[29] S. D. Blunt and K. Gerlach, "Adaptive pulse compression via MMSE estimation," *IEEE Trans. Aerosp. Electron. Syst.*, vol. 42, no. 2, pp. 572–584, Apr. 2006.
[30] S. D. Blunt, T. Chan, and K. Gerlach, "Robust DOA estimation: The reiterative superresolution (RISR) algorithm," *IEEE Trans. Aerosp. Electron. Syst.*, vol. 47, no. 1, pp. 332–346, Jan. 2011.
[31] W. Roberts, P. Stoica, J. Li, T. Yardibi, and F. A. Sadjadi, "Iterative adaptive approaches to MIMO radar imaging," *IEEE J. Sel. Top. Signal Process.*, vol. 4, no. 1, pp. 5–20, Feb. 2010.

Lingyun Ren was born in Sichuan, China, in 1998. She received the B.S. degree in communication engineering and the M.S. degree in communication and information systems from the Nanjing University of Aeronautics and Astronautics, Nanjing, China, in 2020 and 2023, respectively. She is currently working toward the Ph.D. degree in communication and information systems with the Nanjing University of Aeronautics and Astronautics.

Her research interests include signal and information processing and radar imaging.

Di Wu was born in Anyang, China, in 1982. He received the B.S. and Ph.D. degrees in information engineering and communication and information systems from the Nanjing University of Aeronautics and Astronautics, Nanjing, China, in 2005 and 2011, respectively.

In 2011, he joined the College of Electronic and Information Engineering, Nanjing University of Aeronautics and Astronautics, where he worked with the Key Laboratory of Radar Imaging and Microwave Photonics, Ministry of Education, and is currently a Professor. From 2018 to 2019, he was a Visiting Scholar with the Department of Informatics, University of Leicester, Leicester, U.K. His research interests include radar forward-looking imaging algorithms, space–time adaptive processing, and synthetic aperture radar ground moving target indication.

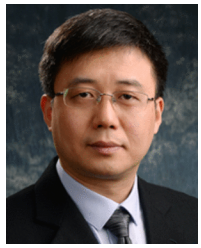

Daiyin Zhu (Member, IEEE) was born in Wuxi, China, in 1974. He received the B.S. degree in electronic engineering from Southeast University, Nanjing, China, in 1996, and the M.S. and Ph.D. degrees in electronics from the Nanjing University of Aeronautics and Astronautics (NUAA), Nanjing, China, in 1998 and 2002, respectively.

From 1998 to 1999, he was a Guest Scientist with the Institute of Radio Frequency Technology, German Aerospace Center, Cologne, Germany, where he worked in the field of synthetic aperture radar (SAR) interferometry. In 1998, he joined the Department of Electronic Engineering, NUAA, where he is currently a Professor. He has developed algorithms for several operational airborne SAR systems. His research interests include radar imaging algorithms, SAR ground moving target indication, SAR/inverse SAR autofocus techniques, and SAR interferometry.